

ARTICLE OPEN



Unconventional resistivity scaling in topological semimetal CoSi

Shang-Wei Lien^{1,10}, Ion Garate^{2,10}, Utkarsh Bajpai³, Cheng-Yi Huang⁴, Chuang-Han Hsu⁵, Yi-Hsin Tu¹, Nicholas A. Lanzillo³, Arun Bansil⁴, Tay-Rong Chang^{1,6,7}, Gengchiau Liang⁸✉, Hsin Lin⁵✉ and Ching-Tzu Chen⁹✉

Nontrivial band topologies in semimetals lead to robust surface states that can contribute dominantly to the total conduction. This may result in reduced resistivity with decreasing feature size contrary to conventional metals, which may highly impact the semiconductor industry. Here we study the resistivity scaling of a representative topological semimetal CoSi using realistic band structures and Green's function methods. We show that there exists a critical thickness d_c dividing different scaling trends. Above d_c , when the defect density is low such that surface conduction dominates, resistivity reduces with decreasing thickness; when the defect density is high such that bulk conduction dominates, resistivity increases as in conventional metals. Below d_c where bulk states are depopulated, the persistent Fermi-arc remnant states give rise to decreasing resistivity down to the ultrathin limit, unlike topological insulators. The observed CoSi scaling can apply to broad classes of topological semimetals, providing guidelines for materials screening in back-end-of-line interconnect applications.

npj Quantum Materials (2023)8:3; <https://doi.org/10.1038/s41535-022-00535-6>

INTRODUCTION

Topological semimetals comprise unconventional materials in which the conduction and valence bands touch at discrete pairs of nodal points or form close-loop nodal lines in the Brillouin zone near the Fermi level^{1–4}. The nontrivial bulk-band topology near the band-crossings yields robust surface states that connect between the nodes, forming open Fermi arcs. Both surface and bulk states contribute to rich transport properties^{5–7}. In the simplest Weyl semimetal comprising two Weyl nodes, carrier transport via the Fermi-arc states resembles that of the edge-states in a stack of 2D quantum anomalous Hall insulators⁸, yielding size-independent contributions to total conductivity at macroscopic scales⁹. In a nonmagnetic Weyl semimetal, if the relaxation lengths associated with the scattering processes between time-reversed partners exceed the sample thickness, similar quantum Hall physics would hold, as if there were two independent Fermi-arc conduction channels⁹.

Furthermore, the increasing surface-to-bulk ratio with reduced sample dimensions should lead to *decreased* resistivity due to Fermi-arc transport¹⁰. Indeed, measurements of NbAs and CoSi appear to support this conjecture: resistivity of ~100 nm thick NbAs nanobelts drops ≥ 10 -fold below its bulk value to $\sim 1 \mu\Omega \text{ cm}$ ¹¹ (lower than bulk Cu resistivity), while that of CoSi nanowires decreases with reduced diameters to $\leq 1/5$ of its bulk value¹². This differs markedly from conventional metals (e.g., Cu) whose resistivity *increases* with reduced dimensions due to carrier scattering off surfaces, grain-boundaries, and so on¹³. The increase in wiring resistance has become a major challenge for advanced semiconductor technologies. In comparison, the resistivity reduction in nanoscale NbAs and CoSi may yield significant performance gains^{14,15}. For example, if the low resistivity observed in the

NbAs nanobelts¹¹ can persist down to the nanometer scale and can be observed in a wider class of materials compatible with silicon technologies, then replacing copper with topological semimetals for wiring up the transistors can improve the power-performance of integrated circuits by at least 10% to ~40%, equivalent to 1 to 4 technology-node generations of performance gain¹⁴, promoting topological semimetals for beyond Cu interconnects among other applications^{15–18}. It is thus imperative to understand the underlying physics and generality of such a resistivity scaling for a broad class of topological semimetals. To this end, we report a rigorous study using a combined first-principles and analytical modeling approach for a representative topological semimetal, the chiral multifermion semimetal CoSi, a material that can be readily integrated in the silicon technology. Our work elucidates the various resistivity scaling regimes in thin films with thickness ranging from 2 to ~50 unit cells and reveals the conditions under which unconventional scaling reverts to conventional metallic scaling.

RESULTS

Electronic structure of CoSi

CoSi is nonmagnetic with a chiral cubic structure (space group # 198) that breaks the inversion symmetry (Fig. 1a). In the absence of spin-orbit coupling (SOC), density-functional theory (DFT) derived bulk band structure reveals a three-fold degenerate band-crossing at Γ and a four-fold degenerate band-crossing at R (Fig. 1c), with Chern numbers +2 and -2 respectively^{19,20}. Consequently, two Fermi arcs (per spin) connect the $\bar{\Gamma}$ and \bar{R} points, spanning the entire projected Brillouin Zone (BZ) along the (100) and equivalent surfaces (Fig. 1d), as confirmed by the angle-

¹Department of Physics, National Cheng Kung University, Tainan 701, Taiwan. ²Département de Physique, Institut Quantique and Regroupement Québécois sur les Matériaux de Pointe, Université de Sherbrooke, Sherbrooke J1K 2R1 QC, Canada. ³IBM Research, 257 Fuller Road, Albany, NY 12203, USA. ⁴Department of Physics, Northeastern University, Boston, MA 02115, USA. ⁵Institute of Physics, Academia Sinica, Taipei 11529, Taiwan. ⁶Center for Quantum Frontiers of Research & Technology (QFort), Tainan 701, Taiwan. ⁷Physics Division, National Center for Theoretical Sciences, Hsinchu, Taiwan. ⁸Department of Electrical and Computer Engineering, College of Design and Engineering, National University of Singapore, Singapore, Singapore. ⁹IBM T.J. Watson Research Center, Yorktown Heights, NY 10598, USA. ¹⁰These authors contributed equally: Shang-Wei Lien, Ion Garate. ✉email: elelg@nus.edu.sg; nilnish@gmail.com; cchen3@us.ibm.com

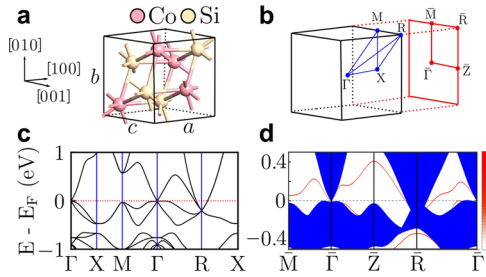


Fig. 1 Crystal structure and band structure of bulk and semi-infinite CoSi. **a** Unit cell of CoSi with lattice constants $a = b = c = 4.438 \text{ \AA}$. **b** Corresponding bulk Brillouin Zone (BZ) and its projection along the (100) surface (shown in red). **c** Bulk electronic band structure of CoSi. **d** Surface-state spectral weight (in red) of a (100)-oriented semi-infinite CoSi slab with the color scale in arbitrary unit. The blue area indicates the bulk bands projected on the (100) surface.

resolved photoemission spectroscopy^{21–23}. In the presence of SOC, each of the doubly degenerate Fermi arcs is split into two. The total number of Fermi arcs extending from near $\bar{\Gamma}$ to near \bar{R} remains the same (4). Therefore, the surface-state contributions to transport would not change qualitatively. Experimentally, since the SOC induced energy splitting is smaller than other broadenings in the CoSi samples, ARPES cannot resolve the Fermi-arc splitting^{21–23}. Thus, within the experimental tolerance, the electronic states near the Fermi level are well described by a model without SOC.

Resistance-area scaling in CoSi slabs with line defects

We first study the DFT informed quantum transport of electrons along the [001] direction in (100)-oriented CoSi slabs of varying thickness, using a 2-terminal device configuration (Fig. 2a) with and without line defects. The slab structure is finite along y and infinite along z , and the transport direction points along x . The line defect in the form of a surface notch extends from $z = -\infty$ to $z = +\infty$ while preserving translational symmetry along z . The self-consistent single-particle Kohn–Sham (KS) Hamiltonian H_{KS} of the scattering region in Fig. 2a is evaluated using the QuantumATK package²⁴. The total conductance per unit area is calculated using the Nonequilibrium Green’s Function (NEGF) technique²⁵ (see “Methods” on ‘DFT-informed quantum transport calculation for CoSi slabs with 1D line defects’).

Figure 2b depicts the Fermi surface of a 40 atomic-layer (AL) CoSi slab (thickness $d = 36.05 \text{ \AA}$), showing that conduction at the Fermi level E_F predominantly comes from the Fermi arcs (denoted by red and blue lines) permeating throughout the projected BZ, while the bulk states (in gray) concentrate near $[0, 0]$ and $[\pi, \pi]$. Correspondingly, the local density of states (LDOS) near the surfaces is significantly higher than the LDOS in the bulk (Supplementary Fig. 2a), and the thinner the slab, the larger the surface- to total-current ratio (Supplementary Fig. 2b). Furthermore, the band structure along a linecut (e.g., L1 along $k_z = 0.52\pi/a$) in the 2D BZ shows that the left- and right-moving Fermi-arc states (S1 and S2) reside on *opposite* surfaces (see top panel of Fig. 2c), resembling the chiral edge states in quantum Hall insulators. Consequently, in CoSi slabs with line defects that preserve the translational invariance along z , if the slab is thick enough such that the top and bottom surface states do not overlap, backscattering between them is *negligible*. This is confirmed in the k -resolved transmission $T(k_z)$ (Fig. 2d), where the transmission remains intact between $k_z \sim 0.4\pi/a$ and $\sim 0.7\pi/a$ despite the surface defect.

Between $k_z \sim 0.2\pi/a$ and $\sim 0.4\pi/a$, multiple Fermi-arc states participate in transport while the bulk conduction is negligible. At a fixed k_z , only an odd number of surface states exist per surface

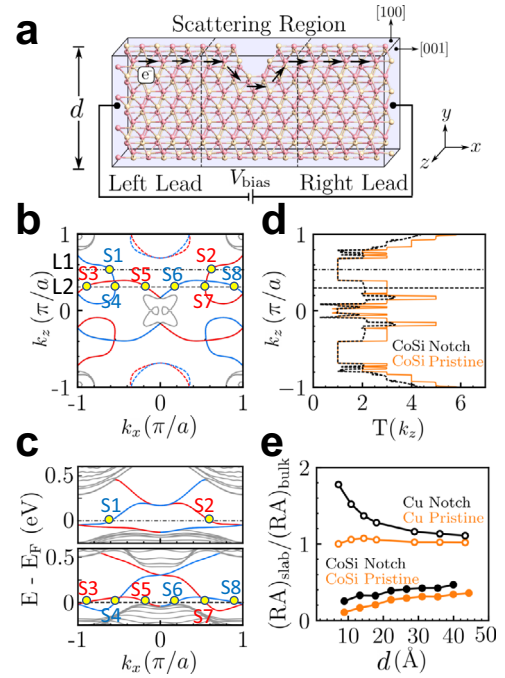


Fig. 2 First-principles informed quantum transport in CoSi slabs.

a Schematic view of a two-terminal device with a scattering region composed of a CoSi slab of thickness d along the [100] direction, sandwiched between two semi-infinite CoSi leads. An external bias-voltage $V_{\text{bias}} \ll E_F/e$ (with e the electron’s charge) injects a charge current in the [001] direction. The arrows illustrate the surface current distribution on the top surface in the presence of defects (shown as a notch). **b** Fermi surface of a 40AL CoSi slab with $d = 36.05 \text{ \AA}$. Fermi-arc surface states on the top and bottom surfaces are denoted in red and blue solid lines, respectively. The dashed lines indicate the topologically trivial surface states, while the gray lines indicate the bulk states. **c** Top panel: band structure of the same slab along the linecut L1 in **b** at $k_z = 0.52(\pi/a) \equiv k_{z1}$, revealing the Fermi-arc surface states (in blue and red) connecting between the bulk valence and conduction bands (in gray). The markers S_1 and S_2 in **b** and **c** indicate the conducting channels available for transport at a fixed k_{z1} . Bottom panel: band structure of the slab along the linecut L2 in **b** at $k_z = 0.3(\pi/a) \equiv k_{z2}$. The markers S_i ($i = 3$ to 8) indicate the conducting channels available for transport at k_{z2} . **d**, k_z -resolved transmission $T(k_z)$ for a pristine 40 AL CoSi slab, compared to that for a slab with a notch on the top surface. **e** Thickness dependence of the resistance-area (RA) product of Cu and CoSi slabs, normalized by the RA product in the infinite thickness limit, denoted as $(RA)_{\text{bulk}}$. The orange curves represent pristine slabs, while the black curves represent slabs with surface disorder in the form of a notch on the top surface. We note that $(RA)_{\text{slab}}/(RA)_{\text{bulk}}$ is equivalent to the normalized resistivity (ρ/ρ_0) as the channel length is fixed in the simulations of the same material.

per spin. For example, along $k_z = 0.3\pi/a$ (L2 in Fig. 2b), there are three states on the top (S3, S5, and S7) and bottom (S4, S6, and S8) surfaces, respectively. Just as S1 and S2, the states related by a C_2 rotation along the z -axis (e.g., S4 and S7) are located on opposite surfaces and cannot backscatter among each other. Nevertheless, S4 can backscatter to S8. Therefore, scattering off a line defect does reduce T (e.g., from 3 to ~ 2 at $k_z = 0.3\pi/a$), but $T(k_z)$ remains larger than one because band topology guarantees an extra forward-moving surface mode for transport. This protected Fermi-arc transmission can be seen in CoSi slabs with various types of line defects (Supplementary Fig. 3).

Figure 2e shows how the Fermi-arc states impact the scaling of resistance-area (RA) product. The number of Fermi-arc channels remains nearly constant with decreasing film thickness, and, at the nanoscale, surface conduction dominates over bulk conduction.

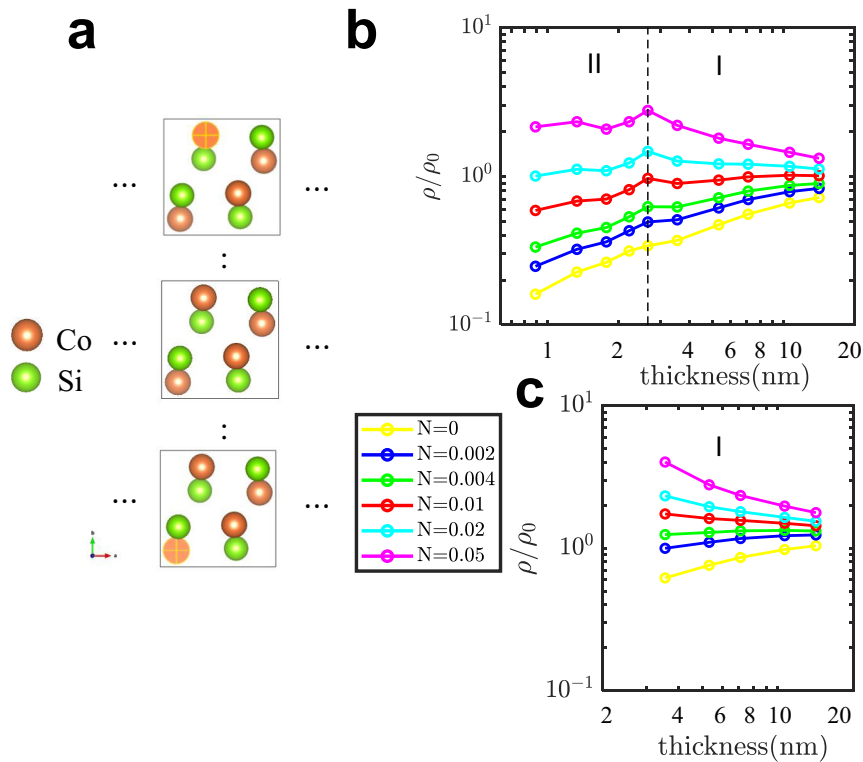


Fig. 3 Resistivity scaling in CoSi slabs with point defects. **a** Crystal structure of a CoSi slab. A yellow cross indicates the position of a surface vacancy point defect. **b** Longitudinal resistivity ρ as a function of the slab thickness, calculated from first-principles electronic structure and Kubo's formula, for different surface defect density N ($N = 0.01$ is equivalent to areal density $\sim 5 \times 10^{12} \text{ cm}^{-2}$). In region *I*, well-differentiated surface and bulk states coexist at the Fermi level. In region *II*, only remnants of the surface states are present at the Fermi level. The resistivity in the infinite thickness limit is denoted as ρ_0 . **c** Longitudinal resistivity ρ as a function of the slab thickness in region *I*, calculated from a combined analytical and first-principles approach (see Supplementary Discussion), for different surface defect density N .

Thus, when thickness is reduced, the conductance per unit cross-sectional area *increases*, i.e., the slab RA *decreases* to well below the bulk RA (see the orange curve with filled circles). This sharply contrasts the scaling in conventional metals, e.g., Cu, where the bulk states carry the conduction and therefore $(\text{RA})_{\text{slab}}/(\text{RA})_{\text{bulk}} \sim 1$ in pristine films even at nanoscale (orange curve with open circles). The contrast is even more drastic when there is disorder: scattering of bulk carriers off surface defects in Cu yields an increasing RA with reduced thickness (black curve with open circles), while the protected transmission of Fermi-arc carriers in CoSi maintains the *decreasing* RA with reduced thickness (black curve with filled circles) despite some loss in transmission. We note that, in the presence of SOC, the split Fermi arcs still extend from near $\bar{\Gamma}$ to near \bar{R} , spanning a large phase space in the BZ. Thus, surface-state transport still dominates. Furthermore, at a fixed k_z , electrons of the split surface bands travel along the *same* direction, and the chiral edge-state like characteristic remains. Thus, the trend of decreasing RA with scaling holds regardless of SOC.

Translational invariance of the line defects ensures that electrons only scatter between the Fermi-arc surface states with the same k_z (see Fig. 2b), resulting in a protected chiral Fermi-arc transport. However, in the presence of point defects, this is no longer true, and an enlarged phase space for scattering leads to a more complex scaling behavior.

Resistivity scaling in CoSi slabs with point defects

When there are point defects, the DFT-informed NEGF calculations become prohibitively expensive. Thus, we perform calculations within the tight-binding formalism by constructing Wannier functions that can reproduce the band structures generated by

QuantumATK (see "Methods" on 'Model Hamiltonians of CoSi bulk, slabs, and vacancies'). This method enables us to extend the relaxation length and conductivity calculations for CoSi films from a few unit-cell to over 100-unit-cell thick. Furthermore, instead of using wave functions explicitly in the Fermi golden rule and Kubo's formula^{26,27}, we adopt Green's functions in the computation in the matrix form (see "Methods" on 'Relaxation length calculations by the Fermi golden rule' and 'Conductivity calculations by Kubo's formula'), which accounts for all matrix-element effects, including suppression of transitions between opposite (pseudo)-spins. This approach speeds up the convergence. It also allows us to introduce an energy broadening factor η (~ 1 meV) as the simplest model for other scattering sources that reduce the lifetime of the entire system uniformly. Next, we introduce Co vacancies on the film surface (Fig. 3a) and construct the corresponding impurity potential and T-matrix (see "Methods" on 'T-matrix calculation'). Cobalt vacancies are used to model the surface defects because their formation energy is lower than Si vacancies. We focus on the impact of surface defects instead of bulk defects because Fermi-arc states dominate the transport of pristine CoSi thin films (Supplementary Fig. 2).

Figure 3b, c summarize the key results of this work: resistivity scaling of CoSi with film thickness (ρ/ρ_0 vs. d) and surface defect density N (defined as the number of defects per unit cell of the slab), where ρ_0 denotes the resistivity of an infinite bulk (see "Methods" on 'Simulation of resistivity vs. thickness scaling'). We observe that, when N is small, ρ/ρ_0 decreases with decreasing thickness d , consistent with the RA scaling in slabs with a shallow notch (Fig. 2e). When N is large, resistivity scales differently above (region *I*) and below (region *II*) a "critical" thickness d_c of 6 unit cells (denoted by the dashed line). Next, we explain this scaling behavior with an analytical model.

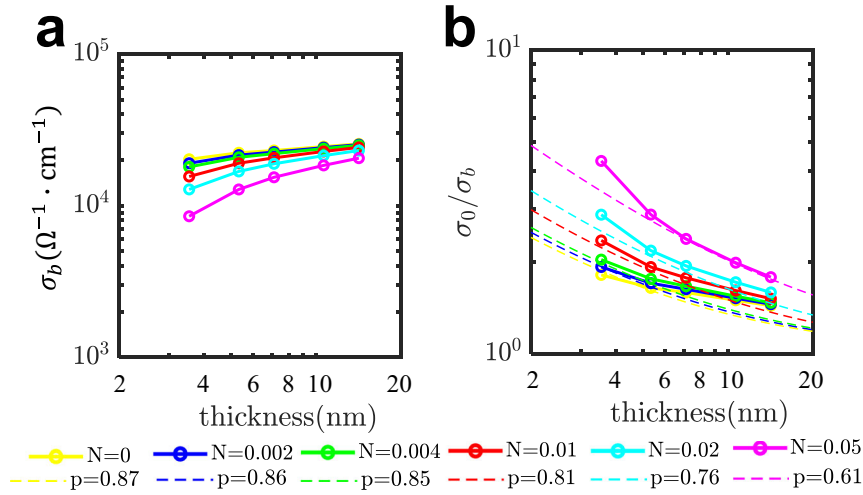


Fig. 4 Scaling of bulk-state conductivity in CoSi slabs. **a** Pure bulk conductivity σ_b (not including the surface state contribution) as a function of slab thickness, for different surface defect density N ($N = 0.01$ is equivalent to areal density $\sim 5 \times 10^{12} \text{ cm}^{-2}$). The range of thickness considered corresponds to region I of Fig. 3. **b** Inverse ratio of the bulk conductivity σ_b to the infinite thickness conductivity σ_0 . The numerical data are fit to the Fuchs–Sondheimer model. The probability of specular surface scattering, p , decreases as N increases.

Resistivity scaling above the critical thickness

When $d > d_c$, well-differentiated surface and bulk channels conduct in parallel and hence $\rho/\rho_0 = \sigma_0/(\sigma_b + \sigma_s)$, where $\sigma_0 = 1/\rho_0$ is the conductivity of an infinite bulk and σ_s (σ_b) is the average contribution from surface (bulk) states to the 3D total conductivity of the film⁹. In this regime, the d -dependence of ρ follows from the competition between two opposite trends.

On the one hand, σ_s grows as d decreases because the number of Fermi-arcs is independent of d . Hence, for thinner samples, Fermi arcs make a higher average contribution to the 3D conductivity. Specifically, an analytical theory developed in Supplementary Discussion shows that

$$\sigma_s = \frac{2e^2}{\pi h} k_0 \frac{l_s}{d} \quad (1)$$

where $k_0 = \sqrt{2\pi}/a$ is the effective length of the Fermi arcs and l_s is an effective relaxation length for surface electrons. Above d_c , l_s hardly varies with d (Supplementary Fig. 4), which can be understood by a dimensional analysis argument (see Supplementary Discussion on “Scaling of relaxation lengths with impurity concentration and system size”). Therefore, σ_s scales roughly with d^{-1} .

On the other hand, σ_b decreases as d decreases (Fig. 4a). Since the 3D bulk mean free path l_0 and the bulk density of states in region I are approximately independent of d (see Supplementary Discussion on “Scaling of relaxation lengths with impurity concentration and system size” and Supplementary Fig. 5), the observed behavior can be attributed to the Fuchs–Sondheimer (FS) mechanism²⁸, namely, the diffusive scattering of bulk electrons from the surfaces. Indeed, the calculated σ_b vs d curves fit well to the FS theory (see Fig. 4b and “Methods” on ‘Fitting to Fuchs–Sondheimer model’).

Which of these two competing trends dominates in the overall resistivity scaling depends on the σ_s/σ_b ratio. Combining Eq. (1) with the FS theory for σ_b , we have

$$\frac{\sigma_s}{\sigma_b} \sim \frac{(e^2/h)k_0}{\sigma_0} \frac{l_s l_0}{d^2 \ln(l_0/d)} \sim \frac{k_0 l_s}{(k_F d)^2} \frac{1}{\ln(l_0/d)} \quad (2)$$

for $l_0 \gg d$, where $k_F \ll 1/a$ is the maximal Fermi wave vector of the bulk crystal for the dominant Fermi pocket. Thus, the main factors enhancing the relative contribution of the surface states to the average 3D conductivity include: (i) long Fermi arcs ($k_0 \gg k_F$),

(ii) long surface relaxation lengths ($l_s \gg d$), and (iii) small film thickness ($d \lesssim k_F^{-1}$). When $N = 0$, we find $\sigma_s/\sigma_b \gtrsim 1$ for the range of d studied (Supplementary Fig. 6), mainly due to $k_0 \gg k_F$ and $l_s \gg d$. In this case, the surface contribution is dominant. Therefore ρ/ρ_0 decreases as d decreases. As N increases, the reduction of l_s and l_0 results in a decrease of σ_s/σ_b (see Eq. (2) and Supplementary Fig. 6). For sufficiently large N , σ_s/σ_b drops appreciably below unity, and the bulk contribution becomes dominant, resulting in the sign change of the slope of ρ/ρ_0 vs d (Fig. 3b, c).

Resistivity scaling in the ultrathin limit

When $d < d_c$ according to Fig. 5, all bulk sub-bands are depopulated. The only states present at the Fermi level are the remnant of Fermi arcs whose wave functions now spread throughout the entire film volume. We note that, contrary to topological insulators, e.g., Bi_2Se_3 , in which the Dirac-cone surface states become gapped in the ultrathin limit due to top-bottom surface hybridization, most of the Fermi-arc states in CoSi remain conducting. This is because, owing to the top-bottom surface asymmetry associated with the CoSi chiral crystalline structure, the majority of the Fermi-arc states from the opposite surfaces do *not* overlap in the \mathbf{k} -space, which protects them from the hybridization-induced gap opening.

For these Fermi-arc remnant states, the 3D conductivity roughly scales as $\sigma \propto \tau/d$, where τ is a scattering time and the $1/d$ factor originates from the fact that the number of remnant Fermi-arc states does not vary appreciably with the film thickness. From Matthiessen’s rule, the scattering rate is a sum of the rates due to surface vacancies and other sources, i.e., $\tau^{-1} \sim a n_{\text{imp}} + b \eta$, where $n_{\text{imp}} = N/d$ is the volume impurity density and a , b are approximately constant. Accordingly, $\rho/\rho_0 = \sigma_0/\sigma \propto aN + b d \eta$ is roughly a linear function of d , with an intercept proportional to N and a slope independent of N . This simple functional form fits qualitatively well to the numerical results in region II of Fig. 3b (see Supplementary Fig. 7). In summary, the Fermi-arc contribution to the 3D conductivity remains remarkably robust down to the thinnest films and thereby enables a favorable resistivity scaling. Similar physics is also observed in the RA scaling of CoSi films with line defects (see Fig. 2e).

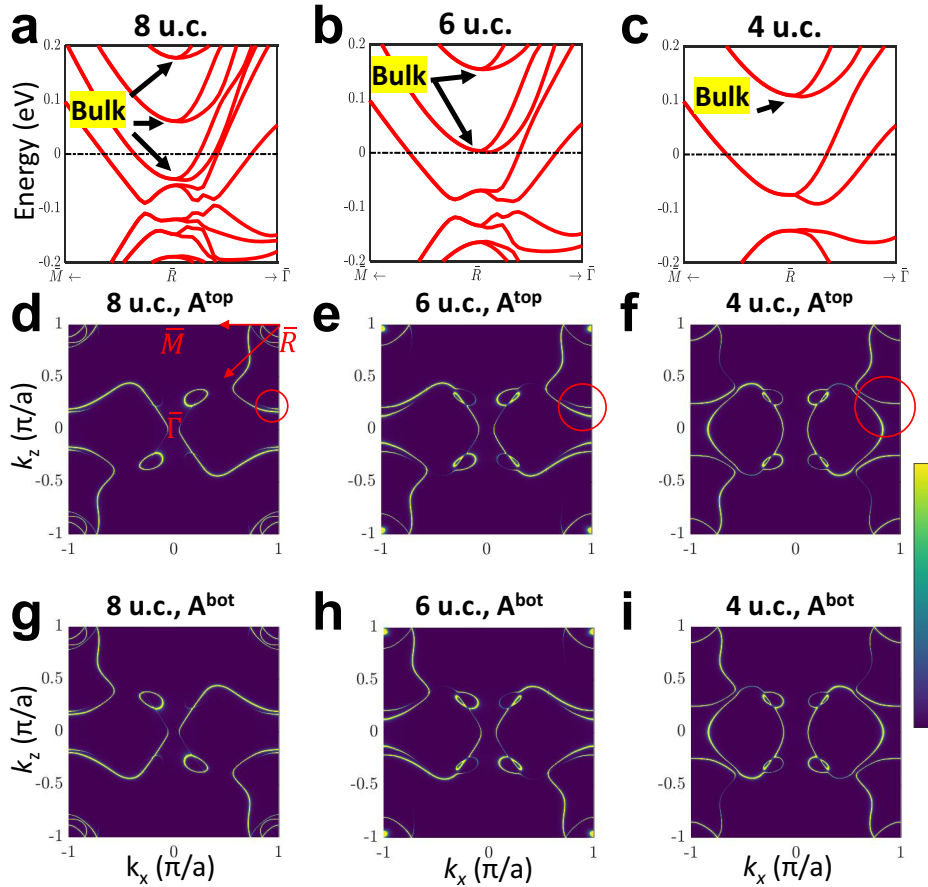


Fig. 5 Band structures and surface-resolved spectral weight of CoSi thin slabs. **a–c** Band structures near \bar{R} , for slab thicknesses of 4 unit cells (u. c.), 6 u. c. and 8 u. c. (respectively). The arrows show the evolution of the bottom of the bulk sub-bands near the Fermi level with decreasing thickness. At the critical thickness of 6 u. c., the bottom of a bulk sub-band crosses the Fermi level, giving rise to a van Hove singularity in the density of states at the Fermi level. Below 6 u. c., the only bands left at the Fermi level are the remnant of the Fermi-arc states. **d–i** Electronic spectral functions of the top 2 layers (A_k^{top}) and bottom 2 layers (A_k^{bot}) in 4 u. c., 6 u. c., and 8 u. c CoSi slabs with the color scale in arbitrary unit. The two spectral functions are related by a C_2 rotation. In the thinnest samples, the Fermi-arc remnant states are spread rather uniformly over the entire film volume, thereby yielding $A_k^{\text{top}} \simeq A_k^{\text{bot}}$. The red circles in **d–f** indicate the splitting of Fermi arcs due to top and bottom surface hybridization. The thinner the slab, the larger the splitting.

Resistivity at the critical thickness

There are two noticeable features in Fig. 3b associated with $d = d_c$. First, in films with a large N , the slope of ρ/ρ_0 vs. d reverses when crossing over from above to below d_c , prompted by the conversion from the bulk sub-band dominated transport to Fermi-arc remnant dominated transport as explained in the preceding discussion. Second, there is a resistivity kink at d_c because at $d = d_c$, the bulk conduction band around R starts to emerge at the Fermi level, giving rise to a van Hove singularity (Fig. 5a–c).

On one hand, the van Hove singularity contributes to more conduction channels, which would increase the total conductivity. On the other hand, the appearance of bulk states at the Fermi level reduces the lifetime for the remnants of the Fermi-arc states, which would decrease the total conductivity. Since the contribution from the emerging bulk states to conductivity is still small at $d \simeq d_c$ (the group velocity of the bulk states at the Fermi level being particularly small at $d = d_c$), the increased phase space for scattering is the dominant factor and gives rise to an upward kink in resistivity at d_c .

According to this interpretation, d_c is generally determined by the thickness below which the bulk sub-bands are completely depopulated and only the Fermi-arc remnant states persist. This

phenomenon is not unique to CoSi, and it would be interesting to validate it in other topological semimetals. We expect the exact values of d_c to depend on the specific materials and the chemical potential of a specific sample. There may also be multiple d_c values if a material has two or more bulk-band valleys near the Fermi level that contribute strongly to transport.

Last, we note that the surface-state penetration depth and the relaxation length associated with the top-bottom surface scattering (l_{tb}) are *not* directly relevant to d_c . While d_c is fixed for a specific material system, the surface penetration depth varies with the wavevector \mathbf{k} . Also, as shown in Fig. 5, the spreading of the surface-state wavefunction at each \mathbf{k} -point toward the opposite surface evolves smoothly across d_c , but the resistivity scaling trend changes abruptly across d_c (Fig. 3b). Furthermore, d_c is a material-specific quantity determined by the electronic bandstructure and Fermi level, independent of the surface defect density N and film thickness d . In contrast, l_{tb} depends on N and d among other factors, and it is several orders of magnitude larger than d_c for the range of N investigated here. These observations corroborate our interpretation that the van Hove singularity associated the emergent bulk sub-band plays a dominant role in determining d_c , as opposed to the spreading of the Fermi-arc surface-state wavefunctions and l_{tb} .

DISCUSSION

We conclude with a discussion on the resistivity scaling of general topological semimetals, focusing on materials with well-separated bulk and Fermi-arc surface states. First, we note the similarities and the differences between the ρ vs. d scaling of the chiral CoSi in Fig. 3b and that of the Weyl semimetal toy model in Fig. 4 of ref. ⁹. In symmetry-protected multifermion semimetals²⁹, such as CoSi, each Weyl node is its own time-reversed partner. Thus, the pair of time-reversed subsystems are strongly coupled. Consequently, instead of a two-step drop in resistivity with a plateau in between that manifests the two channels of anomalous Hall current of the two decoupled time-reversed subsystems in nonmagnetic Weyl semimetals⁹, we see a one-step resistivity drop caused by the dominance of surface conduction over bulk conduction with scaling.

In short, in clean samples with low defect densities N and thicknesses above d_c , the monotonically decreasing resistivity in CoSi is a general feature for nonmagnetic topological semimetals with strongly coupled time-reversed partners, such as chiral multifermion semimetals^{19–23} and Dirac semimetals with Fermi arcs^{30,31}. It is also a general feature for magnetic Weyl semimetals with broken time-reversal symmetry^{32–34}. In contrast, the two-step resistivity decrease shown in ref. ⁹ is a general feature for nonmagnetic topological semimetals with well separated time-reversed subsystems, such as TaAs^{35,36}.

On the other hand, in samples with high N and thicknesses above d_c , the increased resistivity with scaling due to the FS mechanism is a universal feature for most topological semimetals. This is broadly applicable to materials in which the bulk conduction dominates over surface conduction ($\sigma_b/\sigma_s > 1$), as in conventional metals.

Below d_c , where the surface-bulk separation is no longer valid, the decreased resistivity with scaling in CoSi regardless of N is a general feature for topological semimetals with conducting surface states down to the ultrathin limit (see Supplementary Fig. 8), in sharp contrast to prototypical topological insulators, such as Bi₂Se₃, where the topological surface states are gapped out. This property is highly desirable for nanometer-scale interconnects and can be found in topological materials with a sufficiently small overlap between the top- and bottom-surface Fermi arcs in the BZ. Examples include topological semimetals with chiral crystalline structures (e.g., CoSi, RhSi, etc.)^{19,20,37} and Weyl semimetals with asymmetric top and bottom surface terminations, comprising different types of atoms (e.g., TaAs, NbAs)^{35,36,38–40}.

Besides the small coupling between the asymmetric top- and bottom-surface Fermi arcs, other desirable properties that can promote surface conduction include long Fermi arcs (e.g., CoSi, RhSi, AlPt, etc.)^{21–23,37}, many well-separated Weyl nodes, well-separated time-reversed surface-state partners to enhance the surface relaxation lengths (e.g., TaAs), and conduction via chiral-edge-state like Fermi arcs where carriers traveling in opposite directions locate on opposite surfaces to suppress backscattering (e.g., magnetic Weyl semimetals). These serve as the guiding principles for screening topological interconnect materials. Whether or not the abovementioned factors can be satisfied simultaneously is a direction for further research. Detailed analyses of the electron-phonon scattering^{41–43} on resistivity scaling in nanoscale topological semimetals would also be highly valuable.

METHODS

DFT-informed quantum transport calculation for CoSi slabs with 1D line defects

The self-consistent single-particle KS Hamiltonian H_{KS} of the scattering region in Fig. 2a is evaluated using Synopsys'

QuantumATK package, where we employ double-zeta polarized localized orbitals as the basis set and the Perdew-Burke-Ernzerhof (PBE) generalized gradient approximation for the exchange correlation function as introduced in *Phys. Rev. Lett.* 77, 3865 (1996). The slab structures have a finite thickness along the y -direction and periodic boundary conditions in the x - z -plane with a 9×9 \mathbf{k} -point grid that has been checked for convergence. In addition, all structures have been relaxed such that the force on every atom is less than 5 meV/Å.

The zero-temperature total conductance per unit width (G) of the scattering region in Fig. 2a in the zero-bias limit ($eV_{\text{bias}} \ll E_F$) can be calculated using the NEGF technique:

$$G(E_F) = \frac{G_0}{2\pi} \int dk_z T(k_z, E_F) \quad (3)$$

where $G_0 = 2e^2/h$ is the conductance quantum and $T(k_z, E) = \text{Tr}(G^L \Gamma_L G^R \Gamma_R)$ is the k_z -resolved transmission. Here, $G^r(k_z, E) = [E + i\eta - H_{KS}(k_z) - \Sigma(k_z, E)]^{-1} = [G^a(k_z, E)]^\dagger$ is the retarded Green's function, $\Sigma(k_z, E)$ is the self-energy matrix of the left (L) and right (R) leads shown in Fig. 2a, and $G^a(k_z, E)$ is the advanced Green's function. Lastly, $\Gamma_\alpha = i(\Sigma_\alpha - \Sigma_\alpha^\dagger)$ is the level-broadening matrix of lead- α ($\alpha = L, R$).

Model Hamiltonians of CoSi bulk, slabs, and vacancies

The Wannier-type Hamiltonian within the tight-binding (TB) formalism of the CoSi pristine bulk system is derived from the first-principles calculations using the Synopsys QuantumATK package with the d -orbitals of Co and p -orbitals of Si atoms, respectively. In Fig. 1d, we calculate the spectral weight of the surface and bulk states of a semi-infinite bulk using the iterative Green's function, based on the method of cyclic reduction of block-tridiagonal matrices introduced in *Phys. Rev. B* 31, 5166 (1985).

The CoSi slab models with finite thickness d are built with the TB Hamiltonians truncated in the real space along the thickness direction (y). The Co vacancies on the top and bottom surface (Fig. 3a) are modeled by adding an impurity potential V that removes all hopping terms of the Hamiltonian to and from the vacancy sites and setting the on-site energy of the fictitious vacancy atoms to U_0 . The value of U_0 determines the energy of the impurity level, which is unphysical for vacancies. We set $U_0 = 10$ eV above the Fermi level and find that such a high-energy spurious impurity level has negligible effect on the resistivity scaling, as resistivity reflects only the low-energy physics near the Fermi level.

Note that since we consider non-magnetic defects and ignore the SOC, intermixing between spin-up and spin-down electrons is forbidden. When SOC is included, scattering between opposite pseudo-spins would similarly be suppressed. Thus, we expect the resistivity scaling to follow qualitatively the same trend as shown in Fig. 3b.

T-matrix calculation

The impurity potential in momentum space V_q can be obtained by the Fourier transform of the impurity potential in real space. By summing up all diagrams involving multiple scatterings off the impurity, the total scattering matrix $T(\mathbf{k}, \mathbf{k}')$ can be formulated as,

$$T(\mathbf{k}, \mathbf{k}') = V_{\mathbf{k}-\mathbf{k}'} + \frac{1}{N_{\mathbf{k}'}} \sum_{\mathbf{k}''} V_{\mathbf{k}-\mathbf{k}''} G_{\mathbf{k}''}^0(E) T(\mathbf{k}'', \mathbf{k}') = V_{\mathbf{k}-\mathbf{k}'} \left[1 - \frac{1}{N_{\mathbf{k}'}} \sum_{\mathbf{k}''} G_{\mathbf{k}''}^0(E) V_{\mathbf{k}''-\mathbf{k}'} \right]^{-1} \quad (4)$$

where $N_{\mathbf{k}'(\mathbf{k}'')}$ is the total number of $\mathbf{k}'(\mathbf{k}'')$ points; $G_{\mathbf{k}'(\mathbf{k}'')}^0(E)$ is the unfolded bare Green's function at $\mathbf{k}'(\mathbf{k}'')$ point for a given energy E . In this work, when T-matrix is involved, the sum over the momentum space goes up to the second Brillouin zone. Inclusion of the third zone has been tested in a few cases, and less than 10% difference is found.

Relaxation length calculations by the Fermi golden rule

In the Supplementary Discussion, we derive the Fermi golden rule expressions for the relaxation lengths (see Eqs. (28) and (29) in Supplementary Discussion). For first-principles calculations, it is advantageous to use the Green's function instead of wave functions. As a result, Eq. (29) in Supplementary Discussion can be rewritten as

$$\frac{1}{l_{s\bar{s}}} = \frac{2\pi}{a} \frac{1}{N_{\mathbf{k}}} \sum_{\mathbf{k} \in \bar{s}} \text{Im} \left(\text{Tr} \left(G_{\mathbf{k}}^0 \cdot \frac{-1}{\pi} N \cdot \text{Im}(R_{\bar{s}}(\mathbf{k})) \right) \right) \quad (5)$$

$$\frac{1}{l_{sb}} = \frac{2\pi}{a} \frac{1}{N_{\mathbf{k}}} \sum_{\mathbf{k} \in s} \text{Im} \left(\text{Tr} \left(G_{\mathbf{k}}^0 \cdot \frac{-1}{\pi} N \cdot \text{Im}(R_b(\mathbf{k})) \right) \right) \quad (6)$$

where “Im” stands for the imaginary part,

$$R_{\bar{s}}(\mathbf{k}) = \frac{1}{N_{\mathbf{k}'}} \sum_{\mathbf{k}' \in \bar{s}} T^\dagger(\mathbf{k}, \mathbf{k}') G_{\mathbf{k}'}^0 T(\mathbf{k}', \mathbf{k}) \quad (7)$$

$$R_b(\mathbf{k}) = \frac{1}{N_{\mathbf{k}'}} \sum_{\mathbf{k}' \in b} T^\dagger(\mathbf{k}, \mathbf{k}') G_{\mathbf{k}'}^0 T(\mathbf{k}', \mathbf{k}) \quad (8)$$

a is the lattice constant, $N_{\mathbf{k}(\mathbf{k}')}$ is the total number of $\mathbf{k}(\mathbf{k}')$ points in the summation, N is the number of defects per unit cell of the slab, and the indices of s, \bar{s} in Eq. (5) (or s, b in Eq. (6)) denote the mean relaxation length between time-reversed surface states (or between surface and bulk states). The separation of the surface and bulk regions in the Brillouin zone is described in the next section. Last, in Eqs. (5) and (6), the trace Tr is taken over the electronic orbitals in the Hamiltonian matrix.

Separation of surface and bulk states

Because the bulk states can have nonzero spectral weights at the surface and the surface states can mix with the bulk states, in general, a rigorous separation between two cannot be done for finite slabs. Instead, we adopt a practical method to separate the surface and bulk states in the momentum space. The main concept is that any states that appear in the bulk energy gap region (which is forbidden under the 3D periodic condition) must involve surface terminations and have an exponentially decaying wave function amplitude in the bulk, and therefore, those states are defined as the surface states. At each in-plane (k_z, k_x) point, we first identify the conduction-band minimum energy $E_c(k_z, k_x)$ and the valence-band maximum $E_v(k_z, k_x)$ of the three-dimensional (3D) CoSi bulk over all k_y , where y is the out-of-plane direction. We then compute the eigen-energies for each (k_z, k_x) of a two-dimensional (2D) CoSi slab, $E_{2D}^n(k_z, k_x)$, where n denotes the band index. If $E_{2D}^n(k_z, k_x)$ exists in the bulk band gap, i.e., $E_v(k_z, k_x) < E_{2D}^n(k_z, k_x) < E_c(k_z, k_x)$, it is labeled as a surface state; otherwise, it is labeled as a bulk state. Since we only focus on the states near the Fermi level, our method divides the Brillouin zone into two regions: the surface states (inside the bulk band gap) and the bulk states, without any overlap. In some materials, there may exist surface resonances that intermix with the bulk bands. Nevertheless, in CoSi above the critical thickness, the effects of such surface resonances (if any) are negligible, as manifested by the constant density of the bulk states shown in Supplementary Fig. 5.

Conductivity calculations by Kubo's formula

The electric conductivity of a 2D slab system can be computed by Kubo's formula²⁷:

$$\sigma^{2D} \equiv \sigma_{xx}^{2D} = 2 \frac{e^2}{h} \int \frac{d^2 \mathbf{k}}{(2\pi)^2} \text{Re} \text{Tr} \left[\frac{\partial H}{\partial k_x} (G^a(\mathbf{k}, E_F) - G^r(\mathbf{k}, E_F)) \frac{\partial H}{\partial k_x} G^r(\mathbf{k}, E_F) \right] \quad (9)$$

where “Re” stands for the real part, the factor of two is the spin degeneracy, $H_{\mathbf{k}}$ is the TB Hamiltonian of the CoSi slab, $\frac{\partial H}{\partial k_x}$ is the x -

direction velocity operator matrix, the trace is taken over the electronic orbitals of the Hamiltonian, and $G^r(G^a)$ is the retarded (advanced) Green's function,

$$G^r(\mathbf{k}, E) = \frac{1}{E + i\eta - H_{\mathbf{k}} - \Sigma(\mathbf{k})} \quad (10)$$

$$G^a(\mathbf{k}, E) = G^r(\mathbf{k}, E)^\dagger \quad (11)$$

Here, $\eta \sim 1$ meV is a constant that simulates the effect of scattering sources other than surface vacancies (e.g., bulk impurities, phonons, thermal broadening, etc.), and $\Sigma(\mathbf{k})$ is the self-energy matrix:

$$\Sigma(\mathbf{k}) = i \cdot N \cdot \text{Im}(R(\mathbf{k})) \quad (12)$$

$$R(\mathbf{k}) = \frac{1}{N_{\mathbf{k}' \in BZ}} \sum_{\mathbf{k}' \in BZ} T^\dagger(\mathbf{k}, \mathbf{k}') G_{\mathbf{k}'}^0 T(\mathbf{k}', \mathbf{k}) \quad (13)$$

where the real part of the self-energy matrix in Eq. (12) has been omitted, as it can be absorbed into the Fermi energy. The conductivity contributed by the bulk (surface) states, σ_b (σ_s), is derived from Eq. (9) by integrating over the bulk-state (surface-state) \mathbf{k} -points. Note that the impurity vertex corrections are neglected in Eq. (9).

Simulation of resistivity vs. thickness scaling

We normalize the slab resistivity (ρ) against the 3D resistivity of an infinite bulk without vacancy (ρ_0) to obtain the relative resistivity,

$$\frac{\rho}{\rho_0} = \frac{\sigma_0}{\left(\frac{\sigma^{2D}}{d}\right)} \quad (14)$$

Here σ^{2D} is the 2D conductivity of the slab model from Eq. (9); d is the thickness of the slab; σ_0 is the 3D conductivity of the infinite bulk system and can be rewritten as:

$$\sigma_0 = 2 \frac{e^2}{h} \int \frac{d^3 \mathbf{k}}{(2\pi)^3} \text{Re} \text{Tr} \left[\frac{\partial H}{\partial k_x} (G^a(\mathbf{k}, E_F) - G^r(\mathbf{k}, E_F)) \frac{\partial H}{\partial k_x} G^r(\mathbf{k}, E_F) \right] \quad (15)$$

where $H_{\mathbf{k}}$ is the TB Hamiltonian of bulk CoSi.

3D bulk mean free path calculation

We calculate the near-equilibrium carrier transport to estimate the 3D bulk mean free path (l_0). First, we obtain the ballistic conductance G_B of the bulk CoSi system defined as

$$G_B = G_0 \int dE T(E) \delta(E - E_F) \quad (16)$$

where G_0 is the conductance quantum and

$$T(E) = \int dk_y dk_z T(k_y, k_z, E) \quad (17)$$

is the total transmission of the pristine bulk CoSi. In Eq. (16), the δ function is broadened to a Lorentzian of width 1 meV, to be consistent with the 3D infinite bulk conductivity (σ_0) obtained by Eq. (15). Here, the \mathbf{k} -resolved transmission $T(k_y, k_z, E)$ is calculated using the NEFG method (as discussed above for Eq. (3)) with a 300×300 \mathbf{k} -grid-mesh over the Brillouin zone. Next, following the phenomenological expression

$$\sigma_0 = \sigma^B \frac{l_0}{a} \quad (18)$$

introduced in S. Datta's “Lessons from Nanoelectronics: A New Perspective on Transport,” where $\sigma^B = G_B a / A$ and A is the cross-sectional area of the unit cell used to calculate G_B , we can obtain the 3D bulk mean free path as follows for fitting to the FS model in

Fig. 4b:

$$l_0 = \frac{\sigma_0 A}{G_B}. \quad (19)$$

Fitting to Fuchs–Sondheimer model

According to Fuchs–Sondheimer’s theory²⁸, the ratio of the bulk resistivity ($1/\sigma_b$) of the film to that of the infinite bulk ($1/\sigma_0$) can be written as

$$\frac{\sigma_0}{\sigma_b(\kappa)} = \left(1 - \frac{3}{2\kappa} (1-p) \int_1^\infty \left(\frac{1}{t^3} - \frac{1}{t^5} \right) \frac{1-e^{-\kappa t}}{1-pe^{-\kappa t}} dt \right)^{-1} \quad (20)$$

where $\kappa = d/l_0$, l_0 is the 3D bulk mean free path calculated from Eq. (19), d is thickness of the film, p is the degree of specular reflection of the bulk electrons at the surface ($0 < p \leq 1$). Given d and l_0 , we can obtain p by fitting to $\frac{\sigma_0}{\sigma_b(\kappa)}$.

DATA AVAILABILITY

All data needed to evaluate the conclusions in the paper are present in the paper and/or the Supplementary Information. Additional data related to this paper may be requested from the authors.

CODE AVAILABILITY

Code related to this paper may be requested from the authors.

Received: 22 September 2022; Accepted: 16 December 2022;

Published online: 10 January 2023

REFERENCES

1. Lv, B. Q., Qian, T. & Ding, H. Experimental perspective on three-dimensional topological semimetals. *Rev. Mod. Phys.* **93**, 025002 (2021).
2. Armitage, N. P., Mele, E. J. & Vishwanath, A. Weyl and Dirac semimetals in three-dimensional solids. *Rev. Mod. Phys.* **90**, 015001 (2018).
3. Yan, B. & Felser, C. Topological materials: Weyl semimetals. *Annu. Rev. Condens. Matter Phys.* **8**, 337–354 (2017).
4. Bansil, A., Lin, H. & Das, T. Colloquium: topological band theory. *Rev. Mod. Phys.* **88**, 021004 (2016).
5. Hu, J., Xu, S.-Y., Ni, N. & Mao, Z. Transport of topological semimetals. *Annu. Rev. Mater. Res.* **49**, 207–252 (2019).
6. Wang, S., Lin, B.-C., Wang, A.-Q., Yu, D.-P. & Liao, Z.-M. Quantum transport in Dirac and Weyl semimetals: a review. *Adv. Phys. X* **2**, 518–544 (2017).
7. Gorbar, E. V., Miransky, V. A., Shovkovy, I. A. & Sukhachov, P. O. Anomalous transport properties of Dirac and Weyl semimetals (Review Article). *Low. Temp. Phys.* **44**, 487–505 (2018).
8. Burkov, A. A. & Balents, L. Weyl semimetal in a topological insulator multilayer. *Phys. Rev. Lett.* **107**, 127205 (2011).
9. Breitkreuz, M. & Brouwer, P. W. Large contribution of Fermi arcs to the conductivity of topological metals. *Phys. Rev. Lett.* **123**, 066804 (2019).
10. Sukhachov, P. O., Rakov, M. V., Teslyk, O. M. & Gorbar, E. V. Fermi arcs and DC transport in nanowires of Dirac and Weyl semimetals. *Ann. Phys.* **532**, 1900449 (2020).
11. Zhang, C. et al. Ultrahigh conductivity in Weyl semimetal NbAs nanobelts. *Nat. Mater.* **18**, 482–488 (2019).
12. Tsai, C.-I. et al. Cobalt silicide nanostructures: synthesis, electron transport, and field emission properties. *Cryst. Growth Des.* **9**, 4514–4518 (2009).
13. Gall, D. The search for the most conductive metal for narrow interconnect lines. *J. Appl. Phys.* **127**, 050901 (2020).
14. Chen, C.-T. et al. Topological semimetals for scaled back-end-of-line interconnect beyond Cu. In *2020 IEEE International Electron Devices Meeting (IEDM)* 32.4.1–32.4.4 (2020).
15. Gall, D. et al. Materials for interconnects. *MRS Bull.* **46**, 959–966 (2021).
16. Wang, A.-Q., Ye, X.-G., Yu, D.-P. & Liao, Z.-M. Topological semi metal nanostructures: from properties to topotronics. *ACS Nano* **14**, 3755–3778 (2020).
17. Liu, P., Williams, J. R. & Cha, J. J. Topological nanomaterials. *Nat. Rev. Mater.* **4**, 479–496 (2019).
18. Han, H. J., Liu, P. & Cha, J. J. 1D topological systems for next-generation electronics. *Matter* **4**, 2596–2598 (2021).
19. Chang, G. et al. Unconventional chiral Fermions and large topological Fermi arcs in RhSi. *Phys. Rev. Lett.* **119**, 206401 (2017).
20. Tang, P., Zhou, Q. & Zhang, S.-C. Multiple types of topological Fermions in transition metal silicides. *Phys. Rev. Lett.* **119**, 206402 (2017).
21. Sanchez, D. S. et al. Topological chiral crystals with helicoid-arc quantum states. *Nature* **567**, 500–505 (2019).
22. Schröter, N. B. M. et al. Chiral topological semimetal with multifold band crossings and long Fermi arcs. *Nat. Phys.* **15**, 759–765 (2019).
23. Takane, D. et al. Observation of chiral Fermions with a large topological charge and associated Fermi-arc surface states in CoSi. *Phys. Rev. Lett.* **122**, 076402 (2019).
24. Atomistic Simulation Software | QuantumATK - Synopsis. <https://www.synopsys.com/silicon/quantumatk.html>.
25. Datta, S. *Electronic Transport in Mesoscopic Systems* (Cambridge University Press, 1995).
26. Kubo, R. Statistical-mechanical theory of irreversible processes. I. General theory and simple applications to magnetic and conduction problems. *J. Phys. Soc. Jpn.* **12**, 570–586 (1957).
27. Bruus, H. & Flensburg, K. *Many-Body Quantum Theory in Condensed Matter Physics: An Introduction* (Oxford University Press, 2004).
28. Sondheimer, E. H. The mean free path of electrons in metals. *Adv. Phys.* **1**, 1–42 (1952).
29. Bradlyn, B. et al. Beyond Dirac and Weyl fermions: unconventional quasiparticles in conventional crystals. *Science* **353**, aaf5037 (2016).
30. Wang, Z., Weng, H., Wu, Q., Dai, X. & Fang, Z. Three-dimensional Dirac semimetal and quantum transport in Cd₃As₂. *Phys. Rev. B* **88**, 125427 (2013).
31. Wang, Z. et al. Dirac semimetal and topological phase transitions in A₃Bi (A = Na, K, Rb). *Phys. Rev. B* **85**, 195320 (2012).
32. Belopolski, I. et al. Discovery of topological Weyl fermion lines and drumhead surface states in a room temperature magnet. *Science* **365**, 1278–1281 (2019).
33. Liu, D. F. et al. Magnetic Weyl semimetal phase in a Kagomé crystal. *Science* **365**, 1282–1285 (2019).
34. Morali, N. et al. Fermi-arc diversity on surface terminations of the magnetic Weyl semimetal Co₃Sn₂S₂. *Science* **365**, 1286–1291 (2019).
35. Lv, B. Q. et al. Observation of Weyl nodes in TaAs. *Nat. Phys.* **11**, 724–727 (2015).
36. Yang, L. X. et al. Weyl semimetal phase in the non-centrosymmetric compound TaAs. *Nat. Phys.* **11**, 728–732 (2015).
37. Chang, G. et al. Topological quantum properties of chiral crystals. *Nat. Mater.* **17**, 978–985 (2018).
38. Souma, S. et al. Direct observation of nonequivalent Fermi-arc states of opposite surfaces in the noncentrosymmetric Weyl semimetal NbP. *Phys. Rev. B* **93**, 161112 (2016).
39. Xu, S.-Y. et al. Discovery of a Weyl fermion state with Fermi arcs in niobium arsenide. *Nat. Phys.* **11**, 748–754 (2015).
40. Xu, S.-Y. et al. Experimental discovery of a topological Weyl semimetal state in TaP. *Sci. Adv.* **1**, e1501092 (2015).
41. Coulter, J. et al. Uncovering electron-phonon scattering and phonon dynamics in type-I Weyl semimetals. *Phys. Rev. B* **100**, 220301 (2019).
42. Osterhoudt, G. B. et al. Evidence for dominant phonon-electron scattering in Weyl semimetal WP₂. *Phys. Rev. X* **11**, 011017 (2021).
43. Resta, G., Pi, S.-T., Wan, X. & Savrasov, S. Y. High surface conductivity of Fermi-arc electrons in Weyl semimetals. *Phys. Rev. B* **97**, 085142 (2018).

ACKNOWLEDGEMENTS

I.G. acknowledges financial support from the Natural Sciences and Engineering Research Council of Canada (Grant No. RGPIN- 2018- 05385), and the Fonds de Recherche du Québec Nature et Technologies. G.L. acknowledges the support under grant number MOE-2019-T2-2-215 and FRC-A-8000194-01-00. H.L. acknowledges the support from the Ministry of Science and Technology (MOST) in Taiwan under grant number MOST 109-2112-M-001-014-MY3. The work at Northeastern University was supported by the Air Force Office of Scientific Research under award number FA9550-20-1-0322 and it benefited from the computational resources of Northeastern University’s Advanced Scientific Computation Center (ASCC) and the Discovery Cluster. C.-T.C. acknowledges the fruitful discussions with R. Sundararaman, S. Kumar, J. Cha, C. Hinkle, and P. O. Sukhachov.

AUTHOR CONTRIBUTIONS

C.-T.C., H.L., and G.L. conceived the project. S.-W.L., C.-Y.H., C.-H.H., and Y.-H.T. performed the first-principles informed band structures, T-matrix, Green's function, Fermi-golden rule calculations, and quantum transport calculations in consultation with H.L., G.L., T.-R.C., and A.B. I.G. developed the analytical modeling framework; U.B. performed the first-principles informed band structures and NEGF calculations for CoSi slabs in consultation with N.A.L. and H.L. I.G. and C.-T.C. performed the analyses and interpretation of the numerical results using the analytical framework, in consultation with H.L. and G.L. C.-T.C., I.G., S.-W.L., U.B., H.L., G.L., and Y.-H.T. wrote the manuscript. S.-W.L. and I.G. are co-first authors. All authors commented on the manuscript. C.-T.C. oversaw the project.

COMPETING INTERESTS

The authors declare no competing interests.

ADDITIONAL INFORMATION

Supplementary information The online version contains supplementary material available at <https://doi.org/10.1038/s41535-022-00535-6>.

Correspondence and requests for materials should be addressed to Gengchiau Liang, Hsin Lin or Ching-Tzu Chen.

Reprints and permission information is available at <http://www.nature.com/reprints>

Publisher's note Springer Nature remains neutral with regard to jurisdictional claims in published maps and institutional affiliations.



Open Access This article is licensed under a Creative Commons Attribution 4.0 International License, which permits use, sharing, adaptation, distribution and reproduction in any medium or format, as long as you give appropriate credit to the original author(s) and the source, provide a link to the Creative Commons license, and indicate if changes were made. The images or other third party material in this article are included in the article's Creative Commons license, unless indicated otherwise in a credit line to the material. If material is not included in the article's Creative Commons license and your intended use is not permitted by statutory regulation or exceeds the permitted use, you will need to obtain permission directly from the copyright holder. To view a copy of this license, visit <http://creativecommons.org/licenses/by/4.0/>.

© The Author(s) 2023